



Electroluminescent strain sensing on carbon fiber reinforced polymer

J. Qiu^a, M.K. Idris^b, G. Grau^b, G.W. Melenka^{a,*}

^a Mechanical Engineering, York University, Toronto, Canada

^b Electrical Engineering and Computer Science, York University, Toronto, Canada

ARTICLE INFO

Keywords:

Carbon fiber reinforced polymer
Strain and damage sensing
Electroluminescence
Digital image correlation
Piezoresistivity

ABSTRACT

The present paper demonstrates an inexpensive and less labor-intensive machine vision-based strain and damage visualization technique compared to traditional carbon fiber reinforced polymer material inspection methods. This technique is used to characterize the fracture and failure properties upon progressive axial loading in textile carbon fiber reinforced polymer (CFRP) lamina with non-intrusive smart electroluminescent (EL) integration. The smart EL structure utilizes CFRP's unique conductive and piezoresistive properties to visualize deformation and cracks through brightness change. Two fiber orientations ($\pm 45^\circ$ and $0^\circ/90^\circ$) of twill-weave CFRP lamina are fabricated according to a modified ASTM D3039 for linear and fatigue loading in uniaxial mechanical tests to analyze both fiber and matrix-induced EL responses. The EL-strain visualization method is validated with standardized digital image correlation (DIC) utilizing the natural speckling pattern of the EL CFRP lamina. The axial EL-strain results for both static and cyclic loading highly agree with the strain extracted planar conventional DIC strain field on standard and damaged CFRP samples in terms of spatial resolution and sensitivity. This novel strain and damage visualization method aims to be a portable, low-cost, and real-time alternative to non-destructive testing methods commonly used in the composite industry. Instead of periodic checkups, EL architecture allows for real-time strain and damage visualization of composite structure.

1. Introduction

Carbon fiber (CF) composites have been adopted in applications ranging from aerospace to energy due to their high strength to weight ratio, chemical resistance, and both thermal and electrical conductivity [1]. The commercially available CF is manufactured in the form of either polyacrylonitrile (PAN) or pitch-based precursors, in which PAN is the predominant type due to its affordability [2]. Specifically, PAN-based fibers possess higher processibility as it typically comes in the form of textile and braid in different configurations, while pitch-based has much higher electrical conductivity, but harder to handle/process and (e.g. brittle) and expensive. The electrical conductivity of pitch-based (GS-Caltex, Daejeon, Korea) and PAN-based (T-300, Toray, Tokyo, Japan) carbon fiber filaments are $2.20 \times 10^2 \frac{\text{S}}{\text{cm}}$ and $5.88 \times 10^2 \frac{\text{S}}{\text{cm}}$ [3]. However, this is still considerably lower compared to copper filaments, which is $5.8 \times 10^5 \frac{\text{S}}{\text{cm}}$ at 20° Celsius according to IACS (International Annealed Copper Standard) [4]. The PAN-based CF is fabricated from chemical treatment, heating, elongation, and polyacrylonitrile carbonization. CF commonly comes in textile form and can be prepared as a 2D weave or 3D braid, depending on the applications [5].

In the past, the good thermal and electrical conductivity of CFRP is often overlooked compared to its excellent mechanical properties. However, the electrical and thermal properties have recently been utilized for heating of microelectrode applications [6]. Various studies have taken this further as an innovative approach to integrated de-icing [7], lightning strike protection [8], and energy storage [9] in CFRP structures. Utilizing the strain-induced resistance change known as piezoresistive effect in CFRP, a well-established damage location method known as electrical resistance tomography (ERT) has been implemented on CFRP to demonstrate non-destructive damage monitoring [10]. With these desirable characteristics and a reduction in manufacturing and raw material cost, the adoption of CFRP is becoming a more prevalent replacement in a wide range of applications. Despite all the benefits inherent in textile CFRP, its complex fractural and damage mechanics present a difficult challenge to sense damage and predict catastrophic failure in its lifecycle.

Damage in composite materials typically initiates on the micro-scale and then propagates into the macro-scale. The manufacturing process can introduce a broad range of defects; one of the more prominent ones is porosity in CFRP. The presence of voids acts as both stress

* Corresponding author.

E-mail address: gmelenka@yorku.ca (G.W. Melenka).

<https://doi.org/10.1016/j.compositesb.2022.109893>

Received 23 December 2021; Received in revised form 29 March 2022; Accepted 7 April 2022

Available online 12 April 2022

1359-8368/© 2022 Elsevier Ltd. All rights reserved.

concentrations and micro-cracks, which are the initiator for damage propagation. In-service damage in CFRP exists in various forms, such as delamination, fiber-matrix debonding, matrix cracking, fiber fracture, and fiber pull-out. These can be the result of abrupt impact or static and dynamic load [11]. Damage characterizes the state of the structural device. Unlike conventional materials, composite materials exhibit complex failure and damage behavior when exposed to mechanical loading. This behavior is characterized through structural properties via stress and strain acquisition during mechanical loading.

Structural damage sensing methods currently adopted by industry can be categorized into external and integrated [12]. Non-destructive evaluation (NDE) methods such as acoustic emission [13], eddy current [14], Bragg grating [15], thermograph [16], and X-ray [17] are predominantly preferred in the industry as they maintain the structural integrity during operation that minimizes intrinsic detection noise, and can be performed on different scale levels. These NDE acquisition methods can be performed in either contact via surface or embedded sensors and mechanical vibration, or non-contact method such as surface optical measurement via DIC and volumetric computed tomography via microtomography (μ CT) scan. As for the post-failure damage evaluation, this process can be subdivided into detection, localization, and quantification. To elaborate, the damage is initially recognized with health parameters variation. Then the 2D or 3D field of the parameter variations can be reconstructed the damage map to realize the both location and features of the damage. Utilizing the experiment results, a fine-tuned analytical model can be developed to perform damage and failure forecasting. This procedure can be executed in selected interval or in-service inspection, and continuous structural health monitoring (SHM). Different from NDE, SHM has to satisfied three key elements: sensor network, on-board data acquisition and processing, and perform damage evaluation.

For CFRP, ultrasonic inspection has been the industry standard for in-service structural health evaluation. Although ultrasonic testing is staple NDE method for fiber reinforced polymer (FRP) due to its defect detection, volumetric resolution, deploy portability, and low inspection time, it has high material requirements, complex deploy procedure, and heavily relies on operational skill of highly trained personnel for precise examination [18]. The surface NDE inspection method proposed in this study combines the benefit of both conventional NDE and SHM that trade off additional cost on functional layers for simple and fast on-site evaluation, high risk flaw and damage are visually detectable, and has low operational requirement for practitioner.

In contrast, integrated SHM technology implements damage detection and characterization by embedding sensors within the structure or by using the structure itself as the sensor and is a real-time measurement system [17,19]. It is an integrated technique that determines the structural variation of the monitored structure compared to its previous reference undamaged state. SHM is a method that is able to avoid periodic inspections and provides continuous structural surveillance. Although SHM techniques are not currently common for textile composites, but with the increasing implementation of industry 4.0 in composites, there is an urge for combining internet of things (IOT) and real-time SHM that focus on sensing network, interconnectivity, automation, machine learning, real-time data acquisition, and cloud computing to achieve fully autonomous and digital manufacturing [20]. Thus, the benefits of removing human intervention far outweigh the precision and large-scale manufacturing brought forth by the maturity of conventional NDE.

Recently, the electrical characteristic, specifically piezoresistive properties, have been exploited as a damage self-sensing mechanism in CFRP. For instance, the electrical impedance tomography (EIT) method [21] utilizes the electrically conductive nature of CFRP to inject current through designated electrodes and measure the potential difference to visualize damage through mapping [22].

Most continuous damage detection methods only provide a discrete health state of the structure at a specified sensing location. These

methods do not reflect the health state of the entire structure and have measurement sensitivity limited by the number of sensors and their placement. Stress-strain relation in an object or material is a solid mechanics criterion affecting structural health or damage state. A non-destructive and non-contact image-based method can be implemented to monitor the mechanical health states of the structure.

A popular non-destructive vision-based method such as digital image correlation (DIC) is a technique to monitor the strain and damage characteristics of the sample without inflicting variations. DIC is a superficial optical full-field deformation measurement method that operates with a simple image acquisition setup to investigate the complex behavior of composite structures [23–25]. It utilizes tracking of randomized speckles pre-sprayed on the structure prior to mechanical deformation through image acquisition to extract the true strain field [26]. It is proven to be effective and becoming the industrial trend for obtaining a strain field from the textile composite structure during mechanical testing.

Self-sensing is a unique approach to SHM in which the structure itself presents as sensor that generate signal upon reaction to external stimuli [27]. Piezoresistive and piezoelectric material have been a staple in the mechanical testing for strain measurement purpose such as strain gauge [28]. However, the resolution of these methods relies on number of sensors applied. The alternative is to implement sensor on strategic location to predict overall health condition. Blind spots will be a significant disadvantage of these method as exchange for non-intrusive, simple, no processing required implementation. However, the output signal generated by these methods often required post-process to present structure health results. A more comprehensive technique known as electrical impedance tomography (EIT) for piezoresistive is to utilize large data acquisition to perform conductivity mapping of the sample to acquire underlying the strain field [29]. The used of EIT in composite has been limited to damage or anomaly detection in the past. Hassan et al. had utilized a genetic algorithm along with failure criterion on carbon nano-fiber epoxy specimen to predict failure [30]. However, the resolution and efficiency of these method are limited by the number of electrodes, data acquisition, and computational power. Thus, using it for real time monitoring and failure detection need to trade-off between resolution and computational expenses as reconstruction time and resolution exponentially increase with number of electrodes. Later, they focus on two more conventional global search algorithm to evaluate against either with simulation such as finite element analysis or standard strain sensing NDE such as digital image analysis [31].

Mechanoluminescence is perfect a candidate for not only sensing, but visualizing the strain and damage as it emits light upon mechanical excitation such as stress/strain, damage, and friction corresponding to piezo-, fracto-, and tribo-luminescence. Donghyeon et al. embed EuD_4TEA , a fracto-luminescent crystal, in PDMS elastomer to correlate light intensity to high strain-rate compressive loading in high-speed setting for autonomous impact damage detection [32]. However, due to the high-speed nature of fracto-luminescence and the proposed damage detection method, it is unable to continuous monitor the health condition of the structure, let alone localizing the damage. The fact that general fracto-luminescent materials are not structural reinforcement, they have to be attached onto monitored structures to provide estimated structure health results. Donghyeon's group later followed up with split Hopkins pressure test for aerospace application [33]. While Pulliam et al. utilizes the mechanoluminescent properties of ZnS:Cu-PDMS composite to monitor strain induced light emission with counting of illuminating pixel. Although results do shown correlation between tensile strain and illuminating pixel, the method proofs to noisy and inconsistency on tracking cyclic strain for SHM purpose [34].

The EL strain sensing method proposed in this study is comparable to photoelasticity [35], in which strain and stress distribution can be visualized utilizing optical reactive layer. The photoelasticity presents static principal stress or strain in the form of light fringe contours and only limited for transparent or translucent structures such as glass or

plastic. Whereas EL strain sensing expresses stress or strain as global brightness variation and only limited to electrically conductive material.

This paper reports an experimental investigation that validates the feasibility of electroluminescence (EL) full-field strain measurement on piezoresistive structures. Compared to the conventional strain field obtained from the non-destructive DIC method, the aim here is to utilize the EL response of the proposed self-sensing EL CFRP structure to visualize a strain/damage map. Precisely, strain and damage propagation characteristics are studied through axial and off-axis tensile failure and fatigue tests in this work. The naturally randomized EL speckle pattern present in the EL CFRP device is utilized to obtain accurate strain results with the 2D DIC method to validate the EL luminance-strain response. Intrinsic EL is an electro-optic phenomenon in which a doped phosphor material emits light in response to a strong electric field, typically alternating current (AC). Traditionally, EL has been used for lighting applications; however, it is demonstrated here that structural status and EL luminance variation are interrelated. The four-point

probe resistance measurement is employed to monitor the piezoresistive characteristic of each specimen via the resistance change and gauge factor live during each loading tests. The coupled analysis of DIC strain field, EL luminance gradient, and electrical resistance provides a new perspective to study the deformation and damage mechanism. This study proposes a novel continuous SHM method utilizing EL response from the EL CFRP structure while validating the EL-piezoresistive response.

2. Fabrication and acquisition

The EL CFRP structure is a light-emitting capacitor consisting of three main layers: sensing rear electrode, dielectric phosphor illumination layer, and semi-transparent electrode. This structure is comparable to commercial EL lighting strips as illustrated in Fig. 1. Fig. 1 (a) shows the three components of a typical EL illuminating device resembling a resistive-capacitive element. Utilizing the same architecture, the strain-

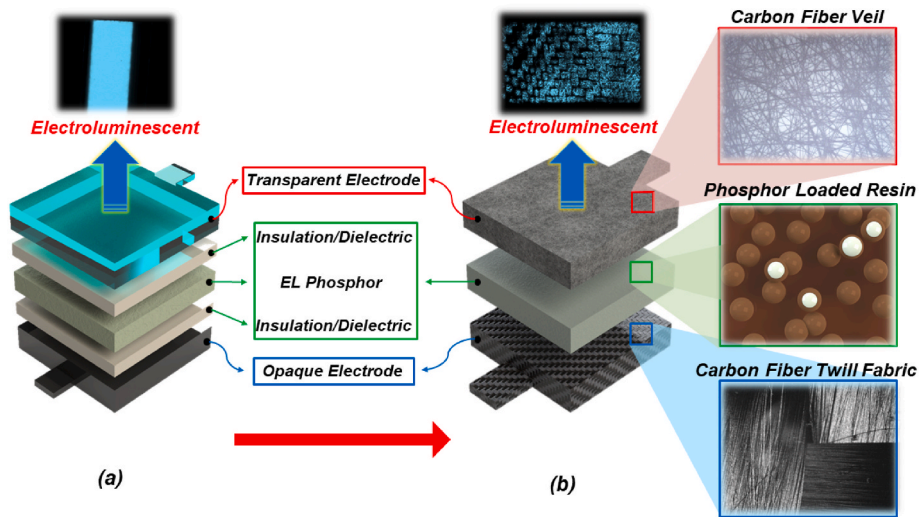


Fig. 1. EL device architectures are illustrated here: (a) conventional EL device compared to (b) strain sensing EL CFRP composite structure with identical layers: transparent electrode, EL phosphor illuminating layer, and opaque sensing electrode.

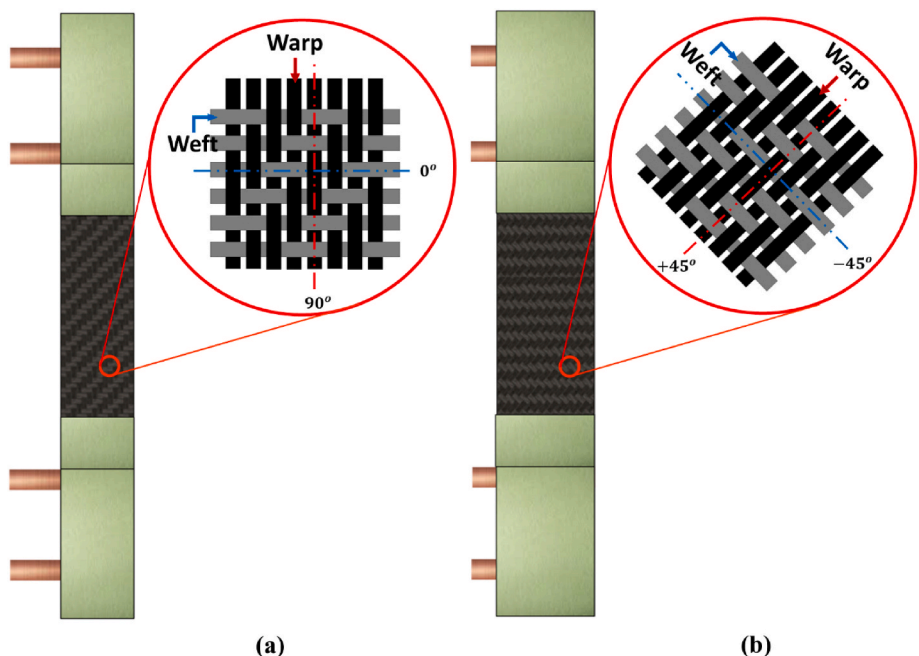


Fig. 2. Textile twill CFRP samples are fabricated in (a) $[0^\circ/90^\circ]$ and (b) $[\pm 45]$ fiber orientation

sensing EL-CFRP architecture studied here is shown in Fig. 1 (b). The sensing rear electrode is a conventional epoxy resin infused woven CF lamina, whose structural state will be detected. The dielectric illuminating layer is epoxy resin loaded with dispersed phosphor powder. It is the sensor module displaying the structural status of the woven CF lamina. The semi-transparent top electrode includes an epoxy resin infused CF veil lamina that allows light to escape for visualization. The overall structure is encapsulated with epoxy resin to contain the entire structure. This design utilizes the electrical conductivity of CF filaments, the capacitive nature of an intrinsic EL device, and the visible light transmittance of the CF veil to enable the SHM capability.

This study focuses on the strain and damage visualization of the CFRP structure under uniaxial tensile loading. Specifically, the different failure modes of CFRP are analyzed through tensile loading both $0^\circ/90^\circ$ and $\pm 45^\circ$ fiber orientation CFRP. Two types of specimens, EL and control, are fabricated in this study. In both variations, only one CFRP lamina is used. To elaborate, the control specimens have one CFRP lamina either in $[0/90]$ or $[\pm 45]$ fiber orientation secured by phenolic endtabs. Similar for EL architecture, one CFRP lamina is used as the bottom sensing electrode with one phosphor dielectric and a CF veil functional layers stacking on top (Note: please refer to Fig. 3 for more specimen detail). We do realize in real application CFRP typically exist in multi-layer laminate system. Since EL is a surficial effect influenced by the conductive layer that contacted with the phosphor layer, thus, performing analysis on a single lamina is representative of a multilayer laminate composite. Since one CFRP lamina is used for all test samples in this study, only in-plane deformation and failure exist during uniaxial tensile testing. Thus, 2D planar DIC is sufficient to capture the tensile loading behavior of this study.

2.1. Materials and fabrication

The CFRP lamina used in this study is fabricated by impregnating woven CF fabric (twill, 6K, CC Fabric) with two-part room temperature system epoxy resin (2000/2060 Laminating System Epoxy Resin, 60-min pot life, Fibreglast). A hydraulic press (10-Ton Shop Press, MAXIMUM) along with two stainless-steel plates (3.5" x 15" Stainless-steel Push Plates, US32D, Rockwood) coated with mold release (Frekote 700-NC Mold Release, LOCTITE®) is used to press form the prepreg CF fabric under 1.45 MPa for 24 h into CFRP lamina with average thickness of 1.24 ± 0.12 mm and surface roughness (R_a) of 1.789 μm .

The CFRP tensile samples are trimmed into both $0^\circ/90^\circ$ (axis loading) and $\pm 45^\circ$ (off-axis loading) fiber orientation strips according to standard ASTM D3039 as shown respectively in Fig. 2 (a) and (b) and the specific dimensions are included in Fig. 3 (a) and (c). The electrical contacts are placed on the CFRP tensile samples in a 4-point probe resistance measurement configuration to monitor the piezoresistive response. The structure of these contacts is shown in Fig. 3 (b). The encapsulating epoxy resin is abrasively removed with P400 and 600 grit sandpaper to reveal the conductive CF yarns. Three coats of silver flake conductive paint (73% Ag Flakes, Acetone Carrier, TED PELCO®) are applied on the revealed region to enhance the electrical contact between CF yarns and rigid electrodes formed from copper sheet metal (24 Gauge, 6" x 12", Copperlab). Four high-strength end tabs with a taper angle of 10° (Phenolic sheet, 0.031" thick, NEMA G-10 Grade, Small Parts) are reinforced at the two ends of test samples with tensile test rated two-part epoxy adhesive (Loctite E-20 Epoxy Adhesive, Hysol™ Henkel) to avoid stress concentration and damage from the grip, prompt the failure to initiate in the middle of the specimen, and stabilize the electrodes.

The planar DIC method utilizes the application of artificial speckles on ASTM D3039 CFRP samples to visualize the 2D strain field during

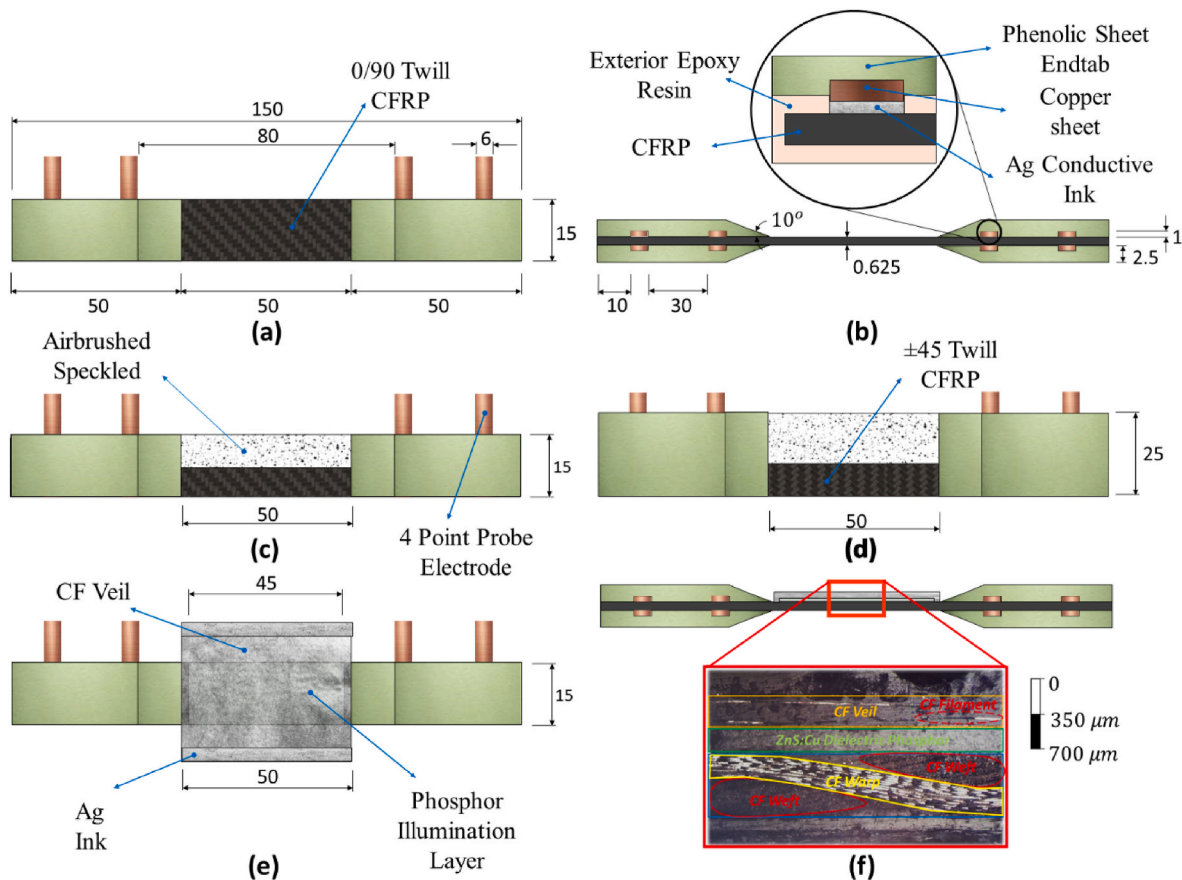


Fig. 3. The ASTM D3039 specimen details in both $0^\circ/90^\circ$ and $\pm 45^\circ$ fiber orientations for (a) and (b) conventional CFRP with 4-point probe electrodes, (c) and (d) artificial airbrushed speckled CFRP, and (e) and (f) EL-CFRP integration.

tensile testing. As indicated in Fig. 3 (c) and (d), the 50 mm gauge length section of both 0°/90° and ±45° ASTM D3039 CFRP samples are first coated with three layers of white base coat (3 M Airbrush Color, Opaque White, 16 oz., Createx) and speckled with black paint (3 M Airbrush Color, Opaque Black, 16 oz., Createx) using an airbrush (Single Action Siphon Feed Airbrush, Paasche) with a 0.5 mm nozzle at 25 psi.

The EL CFRP is a composite structure with two functional layers: transparent electrode and emissive dielectric on top of the ASTM D3039 CFRP specimen as demonstrated in the cross-sectional microscopy image shown in Fig. 3 (e) and (f). A 34.7 μm thick dielectric phosphor emissive layer is blade coated utilizing two layers of acrylic tape (Heavy Duty Acrylic Tape, 3" x 110 yds, 2 Mil, ULINE) as a spacer on the CFRP lamina. The phosphor layer consists of epoxy resin precursor loaded with 70% ZnS: Cu powder. Once the emissive dielectric layer is cured at room temperature for 24 h, the epoxy resin impregnated semi-transparent CF veil (Non-woven Carbon Veil, 10g x 35.5", 0.0021", CC

Fabric) with silver-painted electrodes is overlaid on top and left to cure. The detailed fabrication and characterization procedure of this EL CFRP has been published elsewhere [36]. The fully cured EL CFRP specimen can be activated with 108 V AC at 2 kHz to visualize the overlaying pattern of both woven CF fabric and veil in bluish-green color. A DC power supply (DC Regulated Power Supply, STP3005, 0-30 V/0-5A, SKYTOPPOWER) connected to a DC-AC inverter circuit (EL wire 4xAAA pocket inverter, Adafruit) outputting a variable AC voltage from 99 V to 578 V at 2 kHz is used to drive all EL CFRP specimens used in tensile mechanical tests to similar luminance (32 cd/m²) to accommodate for fabrication variation. The ASTM D3039 CFRP samples loaded in the tensile mechanical tests are categorized by loading direction and design variants as shown in Fig. 3 and Table 1.

2.2. Data acquisition

Table 1
Test specimen specifications

Specimen No.	Specimen Type	Specimen Count	Test Type
D1, D2, D3	B1	3	Constant Excitation Degradation
D4, D5, D6	B1	3	Cyclic Excitation Degradation
D7, D8, D9	B1	3	Environmental Degradation
T1, T2, T3	A1	3	Tensile Failure
T4, T5, T6	A2	3	Tensile Failure
T7, T8, T9	B1	3	Tensile Failure
T10, T11, T12	B2	3	Tensile Failure
C1, C2, C3	A1	3	Cyclic Fatigue
C4, C5, C6	A2	3	Cyclic Fatigue
C7, C8, C9	B1	3	Cyclic Fatigue
C10, C11, C12	B2	3	Cyclic Fatigue

Type A1: CFRP samples with [0/90] lamina and artificial airbrush speckles.
 Type A2: CFRP samples with [±45] lamina and artificial airbrush speckles.
 Type B1: CFRP samples with [0/90] lamina and EL layer.
 Type B2: CFRP samples with [±45] lamina and EL layer.

Fig. 4 (a) shows that the testing apparatus consists of the main tensile test frame, image acquisition, and data acquisition (DAQ) setup. Two tensile test frames, MTS (810 Material Test System, 500 kN loading capacity, MTS) and Instron E3000 (E3000 Linear-Torsion All-Electric Dynamic Test Instrument, ±3000 N dynamic linear loading capacity, ElectroPuls™), are used in this study to accommodate for high-loading static tensile failure and high-frequency dynamic tensile fatigue mode, respectively. Before both loading tests, 100 N of preload is employed to prevent slacking in the specimen. The speckled and EL CFRP specimen is linearly loaded for the static tensile failure test to displace 1.25 mm for 50 mm gauge length (2.5% strain) for 0°/90° specimens and 7.5 mm for 50 mm gauge length (15% strain) for ±45° specimens in the MTS frame over 30 min. The low- and high-frequency regimes are studied separately in dynamic tensile fatigue tests. The low-frequency test is performed by trapezoidal cyclic loading for 6 cycles with 5 min period, and the high-frequency regime is executed with a sinusoidal loading waveform at 20 kHz for 2.5 million cycles for the speckled and EL CFRP within the elastic loading range for both 0°/90° and ±45° specimens.

A charge-coupled device (CCD) camera (Machine Vision Camera, acA2440-35μm, Basler) with a 50 mm focal length lens (Machine Vision Lens, MVL50M23, Navitar) is employed for both speckled and EL

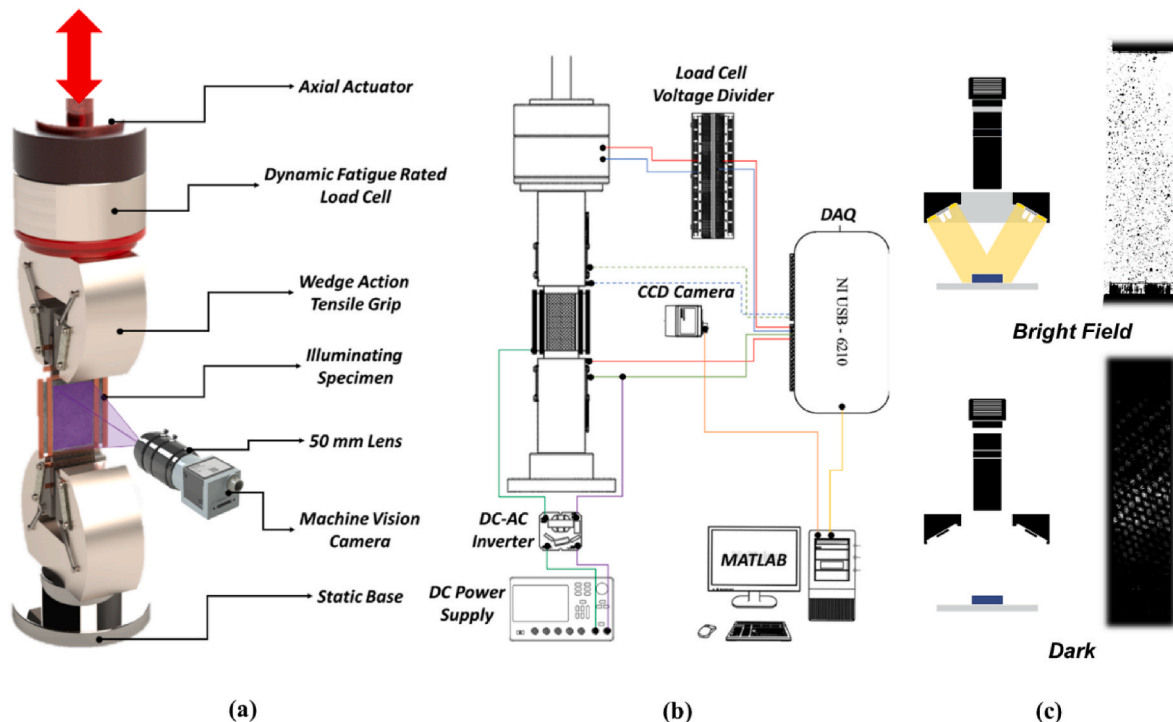


Fig. 4. Uniaxial tensile test setup: (a) tensile test frame, (b) excitation and data acquisition modules, (c) lighting methods for airbrushed and EL samples.

specimens while the tensile test frame is straining the specimen. While both image acquisition setups for speckled and EL specimens utilize a machine vision camera, the light conditions are completely different, as shown in Fig. 4 (c). The bright field illumination method is implemented for the speckled CFRP specimen with two LED panels (*LED Lighting Panel, Adjustable Intensity, 500 Watt, Neewer*) to create a strong contrast between the black speckles and the white base coat. In high brightness acquisition, the aperture size is fixed at $f/2.8$ and exposure time to 0.01 s to prevent overexposure. While the EL CFRP specimen illuminates, a non-reflective enclosed dark environment is required to avoid environmental interference. Since the proposed devices have EL luminance ranging from 32.4 to 35.1 cd/m^2 [37], the aperture size and exposure time are controlled at $f/4$ and 2 s.

The piezoresistive response of both EL and speckled specimens are acquired from copper electrodes with the 4-point probe resistance measurement method to eliminate contact resistance due to contacting interfaces and connections. As illustrated in Fig. 3 (a), the outer electrodes are current injectors, which are connected to a constant current source (*System SourceMeter, 2600B Series, 10A pulse to 0.1 fA and 200V to 100 nV dynamic range, Keithley*), and the inner electrodes are for voltage measurement, which are connected to a DAQ acquisition setup to monitor the resistive change during mechanical straining.

The acquisition setup (see Fig. 4 (b)) consists of two units: the DAQ (*USB-6211, National Instruments*), which obtains all measurements from the tensile test frame and piezoresistive setup, and the image acquisition, which captures image of the samples throughout tensile straining. A custom MATLAB (*R2019b, MATLAB*) application allows the user to control the acquisition parameters and calibration protocol. The integrated loadcells on both the MTS and Instron test frames output the axial stress (σ_{yy}) data by normalizing the load with the average thickness of each test sample. The axial engineering strain (ϵ_{yy}) is obtained through line extraction from the strain field acquired by DIC. The voltmeter electrodes on the 4-point probe resistance setup are utilized to acquire the resistance data. Since this is a noisy measurement setup, the signal is first passed through a digital filter and normalized with initial resistance to obtain the resistance change ($\Delta R/R_0$). To elaborate, the 4-point probe resistance-time response signal is first converted to frequency domain with FFT to identify the high-frequency noise caused by EL excitation primarily at 2 kHz. A digital low-pass filter has been added in MATLAB to remove high-frequency noise. The images acquired by the machine vision camera are used to perform only DIC for speckled samples, but both DIC and EL luminance change ($\Delta L/L_0$) are captured for EL samples. The MATLAB application can directly control the acquisition settings such as exposure time and frame rate with GenTL support from the Image Acquisition Toolbox (*Version 5.5, MATLAB*). The image data acquired by the machine vision camera and stress and resistance data obtained from DAQ are synchronized with time and combined with a MATLAB application to prevent data offset since they have different acquisition rates.

3. Data processing

3.1. DIC

DIC is a full-field, non-intrusive, and rapid method for obtaining in-plane displacement and strain in micro-scale mechanical testing. It has been widely used in the composite industry due to its ease of implementation and well developed and optimized commercial software [38]. DaVis (DaVis 10, CCD image acquisition and processing program, LaVision) is a well-established and comprehensive commercial DIC software capable of performing the preprocessing, correlation, and post-processing of the image stacks in one package. The single camera planar DIC method was implemented here. The implementation of DIC is divided into speckle analysis, camera calibration and acquisition, correlation settings, and post-processing.

The speckle patterns in this study are created through airbrush spray

paint and natural EL illumination. The ideal speckle quality is examined through grayscale level, contrast gradient, density, and size distribution (see Fig. 5 (ii) and (iii)) to ensure the CCD camera can track the speckles accurately during deformation. The natural speckling pattern from EL illumination is generated by the randomly oriented CF filaments from the semi-transparent CF veil electrode on samples with the EL layer. The speckle spatial grayscale level and speckle size distribution are checked since the EL pattern consists of both small speckles and large blobs produced by CF yarns, which can impact the DIC tracking.

The employed CCD machine vision camera is equipped with an IMX250 sensor, which allows for 2448 pixel by 2048-pixel resolution and 3.45 μm pixel size for in-plane displacement measurement. A 95 mm by 112 mm field of view (FOV) with 500 mm working distance is used for all samples to ensure deformation is within the FOV. 12-bit tiff high-resolution images in both high brightness ambient and EL illumination settings are acquired at the rate of 10 frames per second (fps). The excitation voltage for a few initial EL samples were kept under 200 V to avoid shorting the samples, which yields lower luminance and brightness. The exposure time of the camera has to adjust to low brightness acquisition, which in turn limits the frame rate to 1 fps. Later we had realized that high voltage operation does not damage the functional layers, thus higher voltage operation has been adopted to increase brightness of the EL device which improves the operational frame rate of the camera to 10 fps. For consistency among all experiments, the test time has been kept at 30 min despite the large image stack. To accommodate for overwhelming processing time on large image stacks, these 18000 images for each test are reduced to 1800 for an effective 1 fps.

For the image correlation, a rectangular ROI is used on the gauge length of the Type A test samples, but the illumination region is used as ROI for Type B samples (see Fig. 5 (b) and (d)), and this region is subdivided into subsets or correlation windows for cross-correlation or tracking between these subunits. According to guidelines from iDICs [38], 3 to 7 speckles within a window are recommended for optimal correlation. For the best result, the size of the speckle of 3–5 pixels with 50% density within the interrogation window is required. The corresponding recommended step size or overlapping window size is 1/3 of the subset size. This standard is utilized in all mechanical tests with the presence of 3–7 speckles in each subset cell as shown in Fig. 5 (i). The subset size and step size selected for Type A samples are 30 pixels and 7 pixels, as they are sparse and uniform (see Fig. 5 (ii) for (a) and (c)). In comparison, a subset size of 25 pixels and step size of 6 pixels is used for Type B samples, since the speckling patterns are typically high-density clusters (see Fig. 5 (ii) for (b) and (d)). Apart from the speckle density, the conventional airbrushed speckling pattern has much smaller and more uniform speckle size (see Fig. 5 (iii) for (a) and (c)) as compared to EL speckling pattern (see Fig. 5 (iii) for (c) and (d)), which has larger speckle size and lower density. This clustered speckling pattern produced by EL illumination will ultimately reduce the correlation resolution as explain below in discussion.

The commercial software DaVis supports various modes of correlation, and these methods depend on the different reference images. As suggested by iDICs [39], correlation relative to the first image is best suited for low-strain mechanical tests. Thus, relative to first mode is used for type A1 and B1 samples, which consist of $[0^\circ/90^\circ]$ fiber oriented CFRP that only elongates by 2.4% (low strain). Conversely, differential correlation mode is used for the type A2 and B2 samples, which consist of $[\pm 45^\circ]$ fiber oriented CFRP that is typically subject to matrix failure and will elongate by 4.5% and above. Subsequently, the discontinuous mode can be activated to account for discontinuity or larger deformation e.g., crack.

As for the 2D strain field, the displacement data is obtained as a pixel unit. A calibration image is acquired with a physical scale (ruler) placed next to the specimen prior to the mechanical test. In the post-processing stage, the pixel displacement can be converted into physical displacement units. DaVis has adapted the Green-Lagrange strain to calculate the

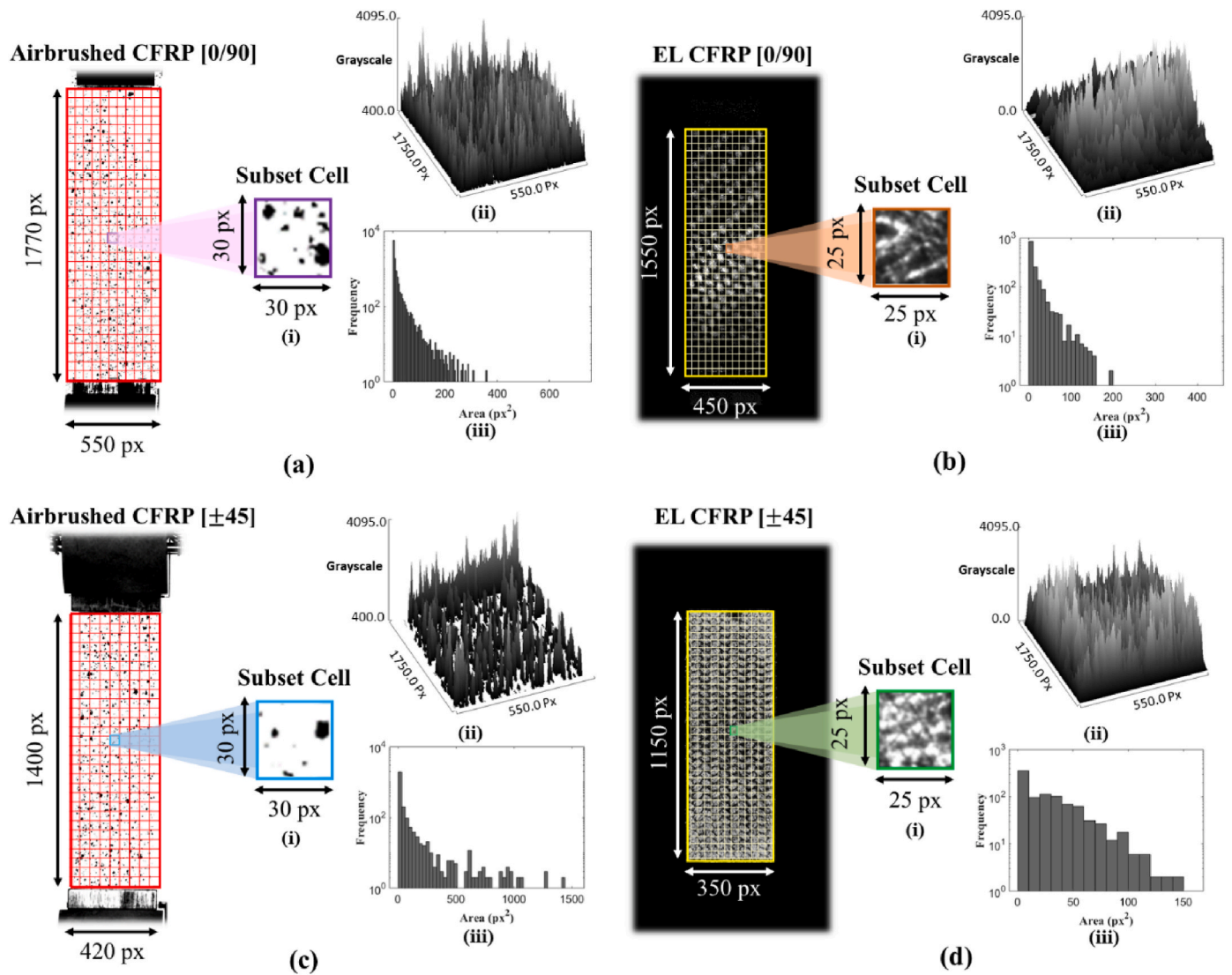


Fig. 5. DIC speckle analysis: (i) subset window, (ii) spatial grayscale, and (iii) size distribution for both [0°/90°] and ±45° CFRP specimens in terms of both airbrush ((a) and (c)) and EL speckling patterns ((b) and (d)).

2D strain field from four displacement gradients: $\frac{du_1}{dx_1}, \frac{du_2}{dx_2}, \frac{dv_1}{dx_1}, \frac{dv_2}{dx_2}$, which are define as axial and transverse strain in x_1 and x_2 directions. These noisy displacement gradients are directed through a low-pass filter, as strain field calculation errors will be significantly amplified with a noisy displacement gradient. Typically for discontinuous samples, subset truncation is applied to prevent the warping of subsets around the crack. This can distort the crack tip shown in displacement fields due to nonlinearity in shape function. A virtual strain gauge is used in the y-axis of the 2D strain field to extract the global ϵ_{yy} strain for each frame.

3.2. EL luminance

The EL luminance is the measured brightness of EL material over its illuminating area. The aim of this analysis is to monitor the EL luminance change of images relative to the first unstrained image to correlate EL luminance change with tensile strain. The EL brightness in the form of grayscale is extracted from images by the machine vision camera. To convert the grayscale digital unit into physical luminance units, a physical benchmark light source, commercially available EL tape strip (*Blue Electroluminescent Tape Strip*, 100 cm, 40 cd/m², 10 nF per meter, *Adafruit*), is used with the same lens and acquisition settings to establish a conversion coefficient. The EL luminance parameter can either be

computed globally or locally. The global EL luminance is defined as the average over the illuminating region motion tracked by a deformable ROI, since most samples will encounter either large deformation or discontinuity. The localized measurement utilizes the same deformable window, but pixel EL luminance is extracted from the image corresponding to a two-dimensional spatial representation of EL luminance response. The EL luminance change is represented as a two-dimensional EL gradient over the pixel space. This study focuses on the correlation between EL luminance and DIC strain in average (global) and 2D (local). The damage location detection aspect was studied in our previous work [36].

The inherent degradation of EL luminance with time and under an applied electric field is investigated to decouple it from the reduction in EL due to mechanical strain. The EL luminance degradation of three newly fabricated specimens each is measured with 578 V AC at 2 kHz for three degradation tests: constant excitation, cyclic excitation, and environmental influence. The constant exaction test is performed by illuminating the EL samples for 180 h of constant excitation under no load and monitoring the brightness degradation due to electrical stress. The electrical stress in this context describes the repeat excitation of the EL device with high voltage, in turn, the dielectric material will degrade and causes brightness reduction. As for the cyclic excitation, the EL

Degradation Characterization

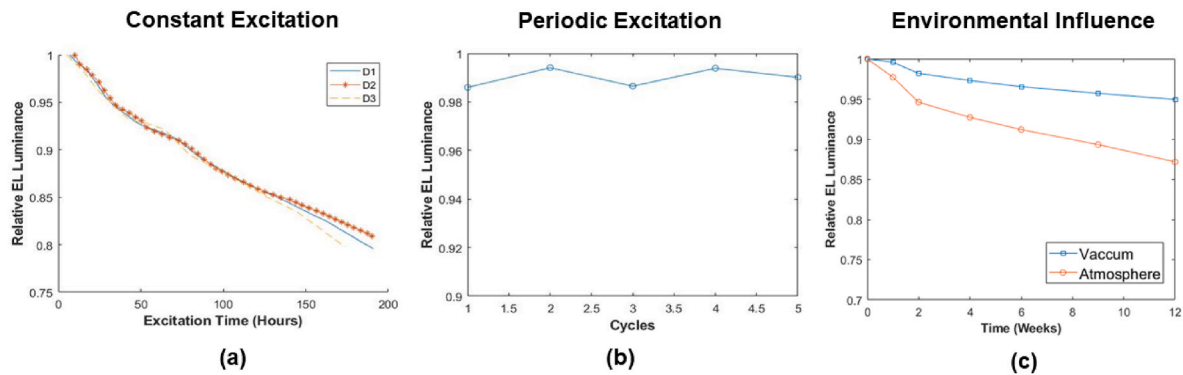


Fig. 6. Degradation analysis for EL samples for (a) constant excitation, (b) periodic excitation, and (c) environmental degradation under vacuum and atmospheric conditions.

sample is illuminated for 1 h and rests for 24 h to allow for full recovery. This one cycle is repeated for five cycles. For environmental test, one EL sample is kept at room temperature and atmospheric pressure condition and a second one is kept in vacuum condition. The moisture and oxidation induced degradation can be measured by comparing these samples after 1 month.

3.3. Piezoresistive characterization

The piezoresistive characteristic of CFRP is studied relying on accurate measurement of the resistance change during both failure and

fatigue tests. A four-point probe resistive measurement is implemented to remove resistance variations due to contacts. As shown in the design configuration (see Fig. 3 (a)), two pairs of copper electrodes are employed on the left and right end of the woven CFRP with the same separation distance. The outer electrodes are connected to a current source, and the voltage is measured between the inner electrodes. The two-point probe is implemented to monitor the contact resistance during each test to ensure rigid connections. The inner electrodes are used simultaneously to measure two-point resistance.

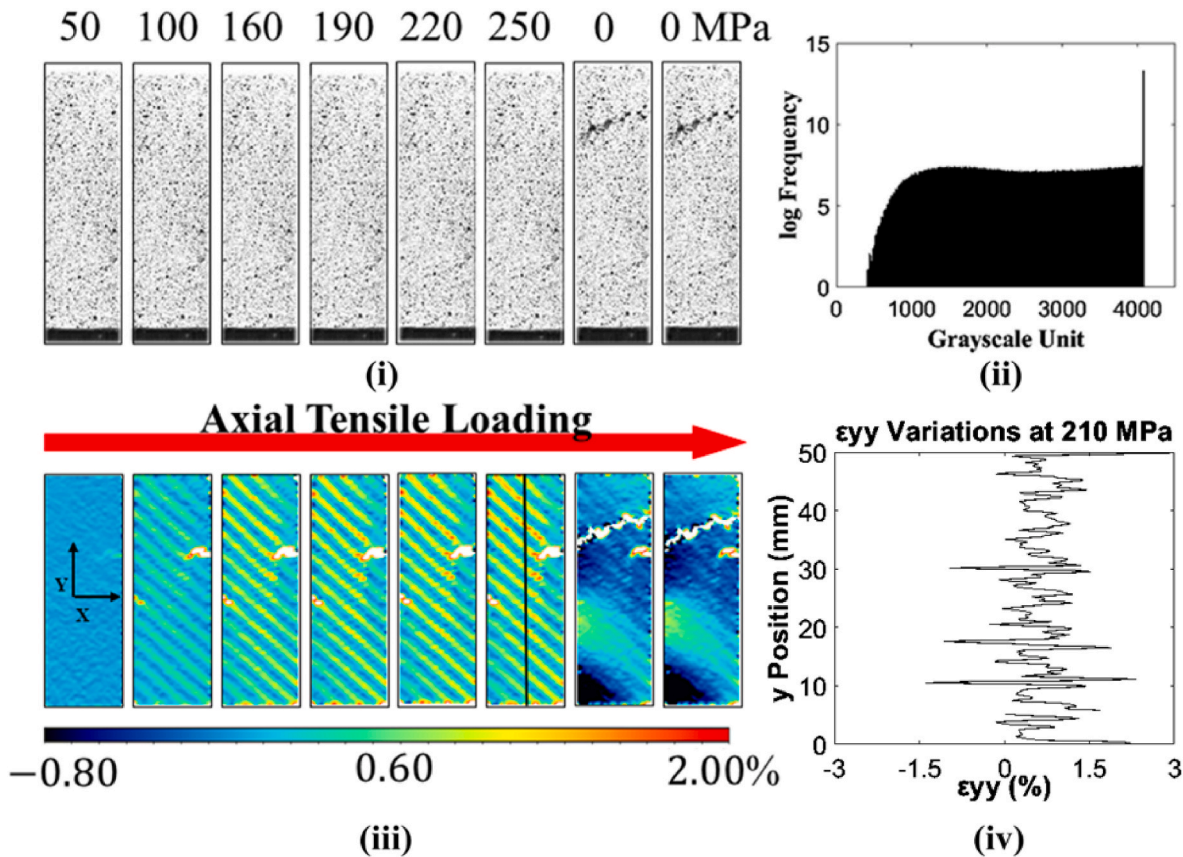


Fig. 7. DIC strain analysis for airbrush speckled $[0^\circ/90^\circ]$ CFRP samples in terms of (i) progressive loading images, (ii) grayscale distribution, (iii) axial strain fields, and (iv) axial strain variations.

3.4. Degradation

The EL luminance response is coupled with degradation, specifically electrical stress and environmentally induced intensity reduction. Thus, these degradation factors are tested here to characterize and decouple them from luminance-strain response. The degradation of the EL luminance is examined in Fig. 6. As shown in Fig. 6 (a), the EL luminance for all three samples decreased by approximately 20% over the duration of 180 h. Therefore, the EL degradation over the duration of a mechanical test, which is 1 h, is negligible. The cyclic illumination response (see Fig. 6 (b)) shows that there is no apparent relation between excitation cycles and EL luminance. This indicates no degradation; thus, no permanent damage is present between excitations, and the EL luminance recovers after each cycle of use. The environmental degradation is illustrated in Fig. 6 (c). The EL luminance of samples exposed to atmospheric condition degrades by only 12% over 3 months (compared with approximately 5% for samples stored in vacuum) (*Isotemp Vacuum Oven, Model 281A, Fisherbrand*), which is minimal due to the epoxy resin encapsulation preventing moisture penetration. These tests illustrate that electrical stress and environmentally induced EL degradation are negligible compared to strain inflicted EL response.

3.5. DIC analysis

The images with their corresponding strain fields captured progressively during axial tensile loading for both conventional and EL implemented CFRP in $[0^\circ/90^\circ]$ orientation is presented in Fig. 7 (i) and Fig. 8 (i) respectively. Since the only loading condition is axial tension, the axial direction strain fields (ϵ_{yy}) are the most representative. As depicted in the axial strain of $[0^\circ/90^\circ]$ CFRP, both artificial airbrushed (see Fig. 7 (iii)) and EL speckling patterns (see Fig. 8 (iii)) display similar

characteristic high strain 45° stripes induced by yarns sliding and matrix cracking due to shearing. Once the tensile straining reaches the ultimate strain (2.3%), both artificial and EL speckled samples fail and display a clean horizontal crack as shown in the 7th image of Fig. 7 (i) and Fig. 8 (i). The splitting or failure of the EL sample due to brittle failure damages all three layers of the EL device, which ultimately disconnects the region furthest away from the current injection terminal and loses illumination progressively, as illustrated in the 6th and 7th image (see Fig. 8 (i)) in the $[0^\circ/90^\circ]$ EL CFRP sample. Inspecting their corresponding strain fields, the correlation remains operational for the artificial speckling pattern, as the speckles are still visible although the sample is detached; whereas the darkening of the bottom region in the $[0^\circ/90^\circ]$ EL CFRP sample causes the disappearance of the speckling pattern and the correlation fails in the detached region (see 7th and 8th image of see Fig. 8 (iii)). The grayscale unit frequency plots indicate speckling density and distribution for both the artificial airbrush and EL speckling patterns (see Fig. 7 (ii) and Fig. 8 (ii)). The final two images for Fig. 7, Fig. 8, Fig. 9, and Fig. 10 (ii) and (iii) in either camera acquisition or DIC strain fields are post failure images of the tensile loading sequence. The corresponding 0 MPa stress on top of the images also indicates occurrence of failure. As for the dark negative compression strain regions shown on the post-failure strain field images in Fig. 7 (iii) are result of recoil of the sample splitting after failure. The larger distribution in grayscale unit and distinct spikes in 4096 grayscale unit indicates weaker contrast between background and speckling pattern for EL compared to the artificial airbrush. This drawback signifies lower resolution and accuracy in correlation, which can be observed in both strain field and axial strain variation plots. Specifically, the strain field is noisier in EL than artificial airbrush speckling, the magnitude of strain variation vs y-position (see Fig. 7 (iv) and Fig. 8 (iv)) are noisier as well. Regardless, the strain fields produced by the EL speckling pattern have sufficient

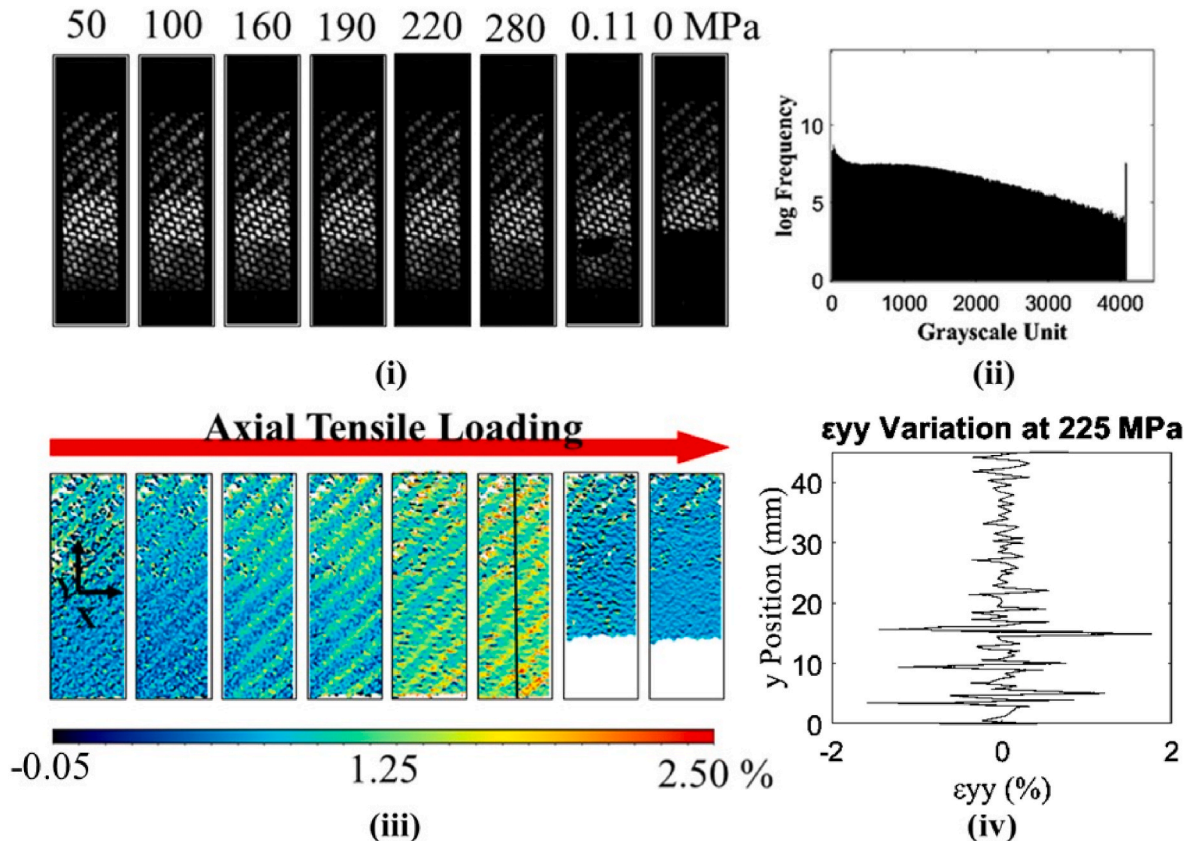


Fig. 8. DIC strain analysis for EL speckled $[0^\circ/90^\circ]$ CFRP samples in terms of (i) progressive loading images, (ii) grayscale distribution, (iii) axial strain fields, and (iv) axial strain variations

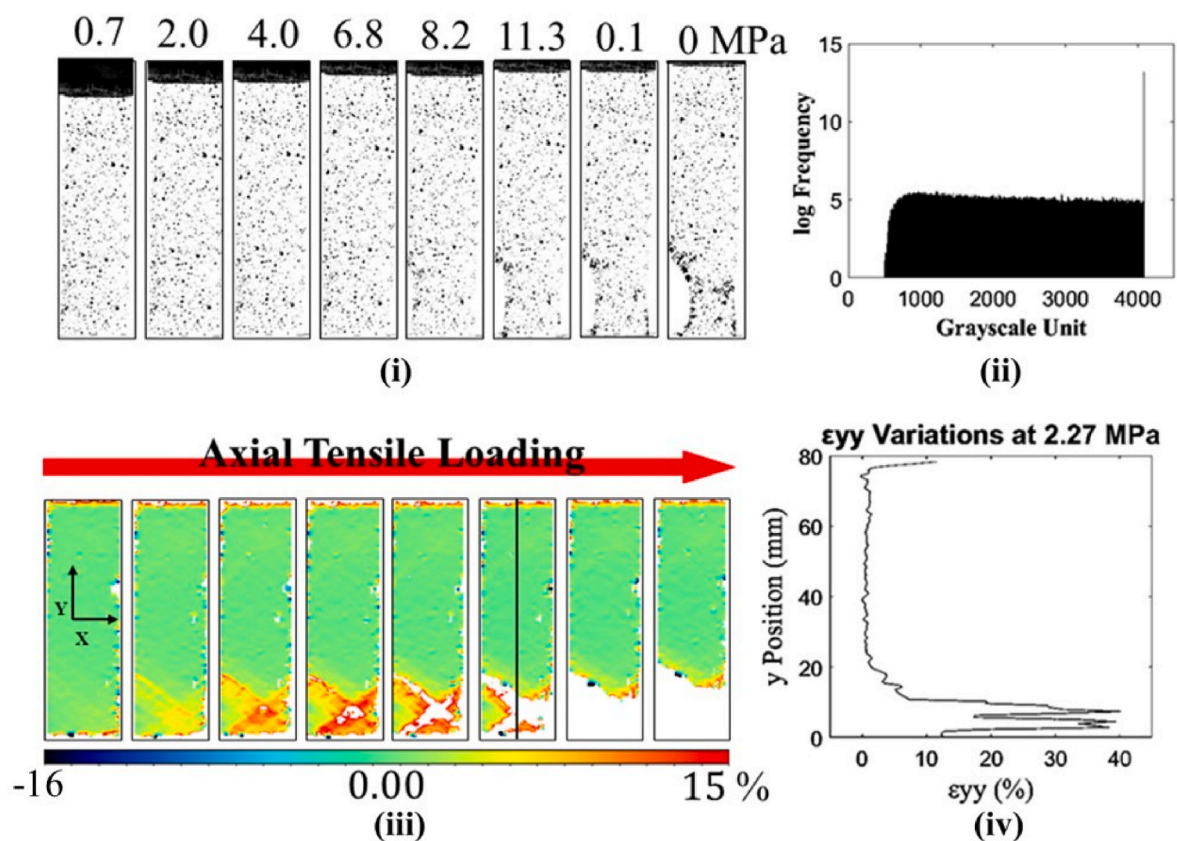


Fig. 9. DIC strain analysis for airbrush speckled $[\pm 45^\circ]$ CFRP samples in terms of (i) progressive loading images, (ii) grayscale distribution, (iii) axial strain fields, and (iv) axial strain variations.

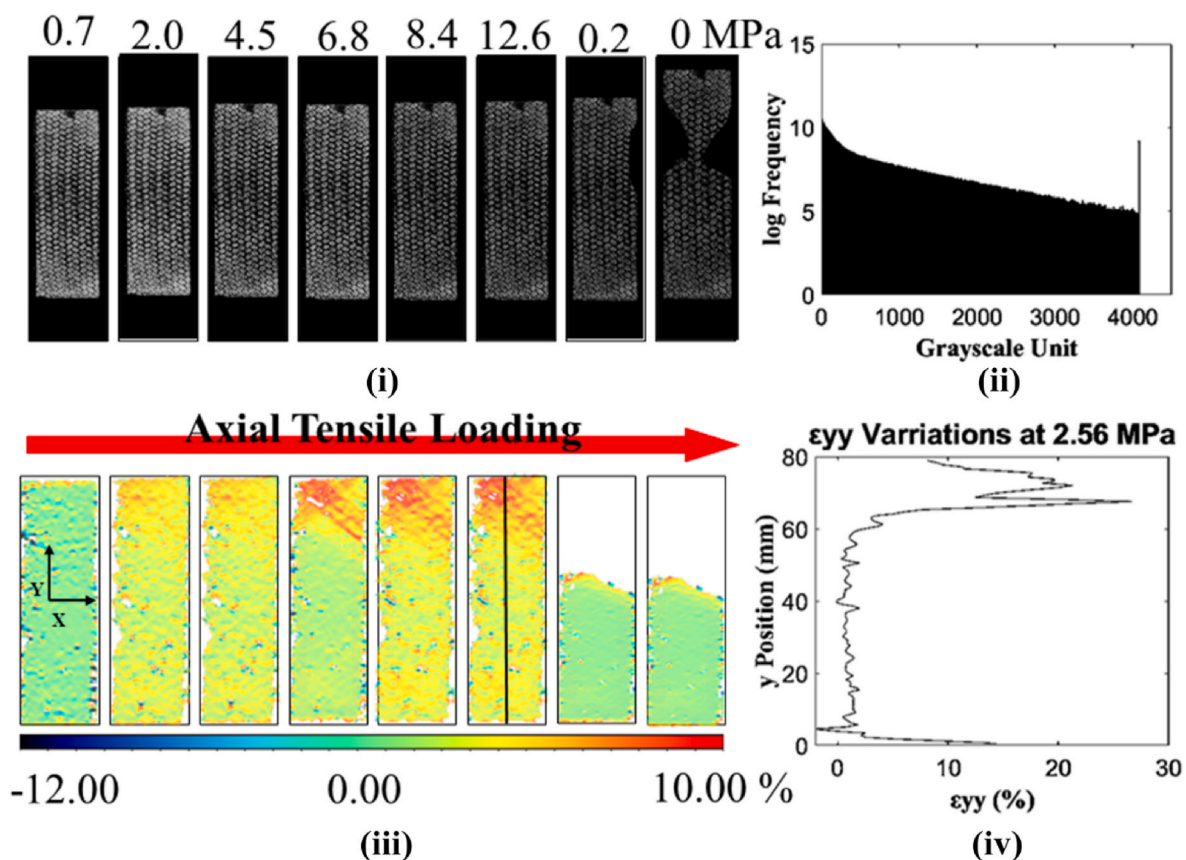


Fig. 10. DIC strain analysis for EL speckled $[\pm 45^\circ]$ CFRP samples in terms of (i) progressive loading images, (ii) grayscale distribution, (iii) axial strain fields, and (iv) axial strain variations.

resolution to correctly identify high strain regions and crack initiation compared to conventional airbrush speckling pattern.

The strain fields and corresponding images for $[\pm 45^\circ]$ CFRP in both artificial and EL speckling patterned samples indicate that these are higher strain samples compared to $[0^\circ/90^\circ]$ (see Fig. 9 (i) and Fig. 10 (i)). The strain fields of both artificial and EL speckled samples display typical matrix failure behavior: samples initiate with uniform zero strain behavior, and transition to high strain in the region where the crack or failure initiates. The matrix failure and crack in the high-strain region are validated from the captured images. Specifically, starting from the 5th image of Fig. 9 (iii) in the artificially speckled sample, the correlation is lost due to matrix cracking and deformation, which can be seen as break-off (ductile failure) of the bottom left corner of the specimen in the 6th image of Fig. 9 (i). The damage then propagates progressively until complete separation, where correlation fails to track the entire bottom section. The EL samples initiate with similar uniform strain field and transition to the high-strain regime in the damage initiation region (see Fig. 10 (i)), but the strain fields shown in Fig. 10 (iii) are noisier compared to the airbrush speckling pattern. The noisy strain field can be validated with y-position axial strain variation, in which the magnitude of variation in the flat section is larger than for the artificial speckling pattern. The tensile stresses are low in Fig. 9 and 10 since the CFRP samples used are off-axis loaded $[\pm 45]$, in which the strongest components CF filaments do not support all the load. The failure mode in these samples are fiber pull-out or polymer matrix cracking, thus, the failure

stress is lower compared to Fig. 7 and 8.

The damage and failure can be predicted through investigating the high-strain region in DIC analysis. This method is applied for $[\pm 45^\circ]$ CFRP, since the separation and crack propagation for the sample is progressive as depicted in Fig. 10 (i). However, the fracture mechanism for $[0^\circ/90^\circ]$ CFRP is spontaneous. Thus, no high-strain region can be visualized in strain fields before failure. Despite the reduction in resolution in planar DIC strain fields for EL speckle compared to airbrushed speckles, the axial strain extracted with both speckling methods is nearly identical as shown in subFig. (iv) of Fig. 7, Fig. 8, Fig. 9, and Fig. 10 for both $[0^\circ/90^\circ]$ and $[\pm 45^\circ]$.

3.6. Tensile failure

The solid mechanics, EL luminance-strain, and piezoresistive responses are correlated in Fig. 11 for both $[0^\circ/90^\circ]$ and $[\pm 45^\circ]$ EL samples. In Fig. 11 (a), the uniaxial tensile test is performed on artificial airbrush speckled and EL $[0^\circ/90^\circ]$ samples until failure, in which all displayed brittle failure between 2.3% and 2.4% strain due to sample variations on the stress-strain relation. The typical ductile stress-strain behavior can be observed for $[\pm 45^\circ]$ EL samples (see Fig. 11 (b)) since the matrix is subjected to axial stress as compared to fiber in $[0^\circ/90^\circ]$. The axial strain extracted from MTS crosshead displacement and artificial speckled DIC strain are nearly identical for both $[0^\circ/90^\circ]$ and $[\pm 45^\circ]$ whereas the EL DIC strain displays fluctuating results due to

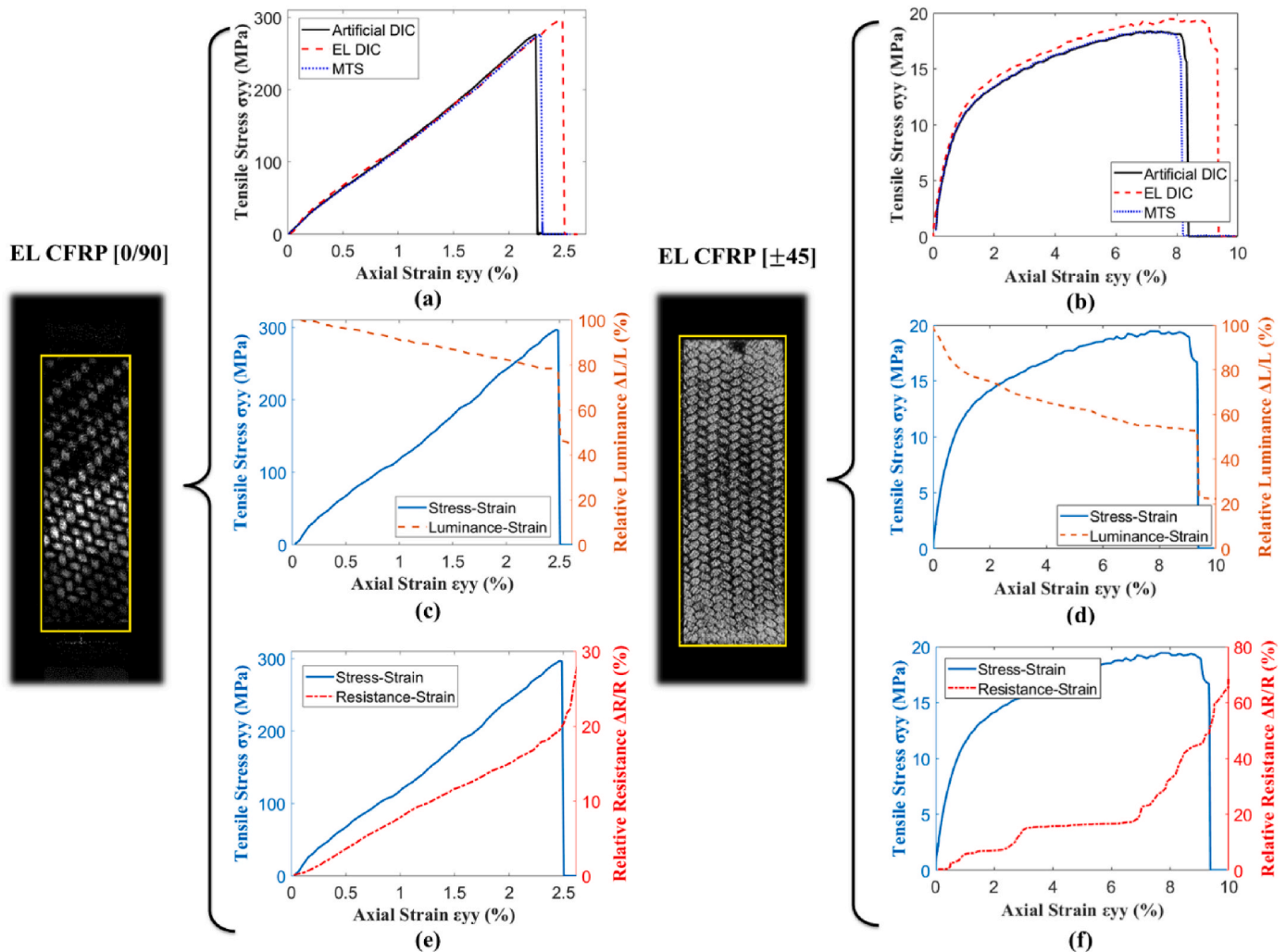


Fig. 11. Linear tensile loading failure results for both $[0^\circ/90^\circ]$ and $\pm 45^\circ$ CFRP specimens in terms of DIC speckling method comparison ((a), (b)), strain-induced global EL luminance change within yellow rectangular ROI ((c), (d)), and piezoresistive response ((e), (f)).

lower strain field resolution in correlation for both cases. The corresponding global EL luminance response induced by axial straining is a steady linear decrease for $[0^\circ/90^\circ]$, which reflects the same behavior as the stress-strain response. As the stress-strain relation abruptly drops to zero due to brittle fiber fracture, the EL luminance response also falls by approximately 28%, and returns to a constant decrease until the fibers are fully detached (see Fig. 11 (c)). As fiber fracture occurs, a clean split is present; if the top electrode does not contact the bottom electrode via an electrical short, the split region closer to the current source will remain illuminating. Thus, the split can be easily identified and located. The EL response for $[\pm 45^\circ]$ also decreases subject to axial straining. However, since the failure mechanics for $[\pm 45^\circ]$ is progressive damage or crack propagation as compared to spontaneous brittle fracture, the EL luminance decrease is gradual and reaches a plateau upon failure as illustrated in Fig. 11 (d). The relation between EL luminance, stress, and strain response shows strong agreement through the repetition of three specimens only with minor differences at the location of splitting and EL luminance plateau. The piezoresistive response for tensile axial loading in $[0^\circ/90^\circ]$ shown in Fig. 11 (e) is linear prior to failure. Once the specimen reaches failure strain, fiber fracture occurs, thus increasing the number of broken filaments. Fiber breakage causes a more drastic resistance change compared to fiber elongation, which is only a geometric change. The relative resistance response for $[\pm 45^\circ]$ samples increase with straining in steps due to progressive damage, and larger steps after failure, as depicted in Fig. 11 (f). As the matrix failure is initiated, fiber pull-out and matrix cracking will take place. In turn, the empty air gaps caused by fiber pullout will increase the resistance in large magnitude steps.

3.7. Tensile fatigue

The tensile fatigue tests are performed in both low- and high-frequency regimes (see Fig. 12 (a)) to validate the axial strain induced EL response and investigate the fatigue failure for both piezoresistive and EL response for the $[0^\circ/90^\circ]$ samples. The six cycles of triangle waveform input strain transient response used in the low-frequency cyclic fatigue tests (see Fig. 12 (b)), show good agreement between the three samples with slight variation in strain peaks due to fabrication differences. The EL luminance transient response shown in Fig. 12 (c) has an amplitude of 5.2% luminance change and is out of phase from the input triangle loading waveform by a half period, i.e., maximum strain corresponds to minimum EL luminance. The EL luminance also shows a constant degradation trend of 0.2%, which is negligible. In addition, the response is noisy due to the low frame rate of the CCD camera under high exposure time conditions. This can be resolved by increasing the EL brightness with voltage increase or prolonging the period for each cycle to acquire more image data. As for the piezoresistive response (see Fig. 12 (d)), the cycle amplitude is 1.5% with initial resistance of 1.32Ω . Unlike the EL luminance response, the piezoresistive response is in phase with the triangle loading input. Unlike the low-frequency fatigue test which kept the cycling loading amplitude within the elastic range, the high-frequency fatigue test cycles the sample with amplitude of 2500 N for 2.5 million cycles reaching fatigue failure. As observed in Fig. 12 (d), the EL luminance response decreases in sharp steps with axial fatigue cycles due to brittle failure and delamination of the phosphor illumination layer, and ultimately reaching complete darkness. The purpose of fatigue testing is to demonstrate an elongated result of tensile cyclic test, thus, only $[0/90]$ sample has been tested as $[\pm 45]$ does not illustrate piezoresistive effect.

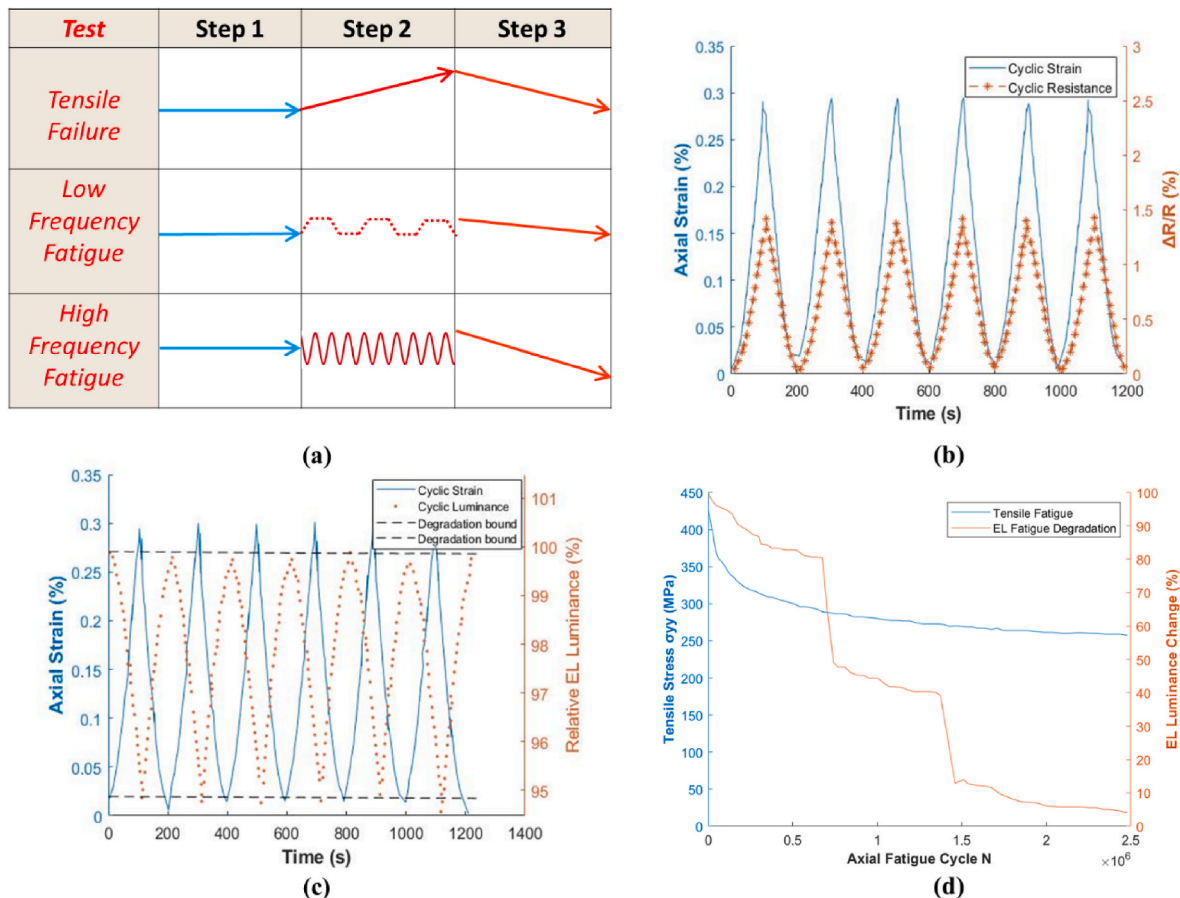


Fig. 12. Tensile fatigue test results: (a) Test details, (b) cyclic strain vs time response, (c) EL-cyclic strain vs time response, and (d) fatigue EL-degradation response.

Table 2

Mechanical properties and failure characteristics for all CFRP specimen types under tensile loading. A1: [0°/90°], conventional CFRP; A2: [±45°], conventional CFRP; B2: [0°/90°], EL; B2: [±45], EL.

Specimen Type	Thickness (mm)	Failure Strain (%)	Ultimate Strength (MPa)	Young's Modulus (MPa)	Gauge Factor	Luminance Strain Factor
A1	1.10 ± 0.09	2.28 ± 0.17	284.14 ± 10.77	12582 ± 332	6.81 ± 1.22	N/A
A2	1.38 ± 0.22	8.23 ± 1.18	17.83 ± 2.41	4067 ± 385	N/A	N/A
B1	1.89 ± 0.89	2.39 ± 0.22	298.42 ± 14.20	13592 ± 246	6.14 ± 1.38	7.78 ± 1.38
B2	2.14 ± 0.62	9.89 ± 0.96	19.14 ± 8.74	3695 ± 359	N/A	5.41 ± 0.51

4. Discussion

Four types of samples are fabricated in this study, which are indexed by A1, A2, B1, B2. The letter A and B represents the type of architectures: A for unmodified and B for EL modified samples. The number 1 and 2 indicates the fiber orientation of CFRP: 1 for [0°/90°] and 2 for [±45°]. The mechanical, EL luminance, and gauge factor for destructive tensile-failure tests for all these samples are detailed in [Table 2](#).

The material properties, namely the failure strain, ultimate strength, and elastic modulus obtained from brittle tensile failure tests on EL-CFRP as shown in [Table 2](#) are comparable to press-cured [0°/90°] CFRP lamina [40]. The material properties with [±45°] fiber orientation for both EL and control CFRP display significantly higher failure strain and lower ultimate strength due to off-axis loading, which mainly strains the epoxy resin matrix. A slight increase in ultimate strength for EL-CFRP can be explained with the thicker sample with additional functional and illuminating layers as the tensile stress was calculated using only the thickness of the structural CFRP electrode, not the sensing EL layers. The gauge factor defines the ratio between resistance change and strain. The results obtained here are comparable with Khalid et al. [41]. The [0°/90°] samples in both forms (A1 and B1) exhibit a linear strain-resistance relation producing a similar gauge factor of 6. However, the [±45°] orientation does not show a linear relation between strain and resistance change, since the resistance change is predominately controlled by spontaneous fiber pullout and matrix cracking between yarns. Recent advances in alternating current activated EL devices had focused on stretchable EL polymers with flexible conductors [42]. Wang et al. investigated PDMS based ACEL devices. They found EL luminance initially increases by up to 280% with stretching due to dielectric thinning, and ultimately reduces back to 70% for large strain [43]. A comparable luminance reduction effect (~88%) can be seen for silver nanowire network electrodes and urethane acrylate matrix ACEL devices for 120% axial strain [44]. The reduction in luminance with strain may be due to a reduction in phosphor density and for nanowire electrodes may be due to a reduction in electric field intensity in the open areas between nanowires where light is emitted [43]. The EL luminance is utilized in this paper to visualize the mechanical strain in a rigid, less elastic conductive CFRP sample with much lower strain (2.5–10%). In this case, the reduction effect is much more prominent compared to the increase in EL luminance. Thus, a luminance-strain factor similar to gauge factor is developed to characterize the relative EL luminance changes due to mechanical strain in this architecture. The average luminance-strain factor for [0°/90°] samples is around 7.78 for 3 samples, indicating a 18% luminance decrease with 2.39% axial strain in the linear elastic region, which can hardly be detect by human eyes. The [±45°] EL samples exhibit a much higher luminance change of 46% with 9% strain, resulting in a luminance-strain factor of 5.41. Thus, the larger luminance change in [±45°] EL samples can be detected by human eyes. The gauge factor and luminance-strain factor for [0°/90°] are similar. Conversely, a linear gauge factor cannot be extracted for [±45°] samples, but they have high luminance-strain factor. Compared to industrial standard ultrasound damage characterization method, which can inspect through both surface and thickness of samples without material limitations, the EL architecture and its

Table 3

Mechanical properties per unit weight comparison between EL-modified and non-modified [0°/90°] CFRP samples

CFRP Types	Weight (g)	Normalized Ultimate Strength (MPa/g)	Normalized Tensile Modulus (GPa/g)
Non-modified	5.90	48.16	2.13
EL-modified	6.24	47.82	2.18

luminance-strain factor proposed in this paper allows for visualization of the surface mechanical strain in only electrically conductive textile composites. The tensile modulus and strength are lower compared to other works due to the limitations in fabrication technique and modification on ASTM D3039 standard such as fiber misalignment and distortion, as well as thicker samples with excess epoxy compared to others. For this work, our focus is to demonstrate the effectiveness of the EL sensor. A follow up study is required for full ASTM D3039 samples as well as structural components to further develop the method outlined in this manuscript.

As seen in [Table 3](#), no significant magnitude of difference can be identified mechanical properties such as failure strain, modulus, and ultimate strength between EL modified and unmodified CFRP samples as shown in the table. Thus, this result confirmed the fact that this method is non-intrusive or in another words, the addition of functional layers does not change the structural identity of CFRP sample. As measured in the table above, the modified functional EL layers only contribute 5.4% of the overall weight. Although there are variations in both normalized ultimate strength and tensile modulus between non-modified and EL-modified CFRP, they are only 0.7% and 2% respectively. The variation is a combination of both sample variation and EL-modification, in which both have negligible effect on the mechanical properties.

An additional study has been performed to verify no heating is present with the high voltage and corresponding current input. Since only high voltage is applied between electrodes, but the current is relatively low, thus, the overall power is not sufficient for significant heating. For further investigation, an IR temperature monitoring for 1 [0/90] EL CFRP sample during EL excitation is included in [Table 4](#).

Table 4

Temperature monitoring of [0°/90°] EL CFRP device

Excitation Time	Temperature
1	19.2
2	20.1
3	19.8
4	19.3
5	20.4
6	20.2

5. Conclusion

Here, the fabrication process and SHM capability of an innovative self-sensing EL CFRP is demonstrated. The proposed fabrication process is compatible with traditional CF composites for self-sensing. The self-sensing of the proposed structure is achieved through monitoring of EL luminance and four-point resistance response induced by deformation and damage in tensile failure and cyclic fatigue tests. Utilizing 2D planar DIC, EL, and four-point resistance, the mechanical strain-induced EL luminance and piezoresistive relations are established. Based on the experimental results, both the relative resistance and EL luminance change follow the waveform loading input, in which the resistance and EL response indicates strong correlation with input strain. Upon failure, the EL luminance response shows a sharp drop indicating darkening of the damage region. At failure, the resistance increases sharply, revealing the occurrence of fiber breakage. This study provides a novel, non-destructive SHM method for real-time inspection of any CFRP component. It can detect, locate and characterize strain and damage in conventional CFRP structures.

The work flow of conventional non-contact NDE is broken down into signal acquisition, processing, and result visualization. The raw signal output from conventional non-contact NDE and self-sensing techniques is fragmented and noise-filled. Thus, these methods require additional equipment and service for signal processing and present results for user. The proposed EL architecture merges strain and damage signal process and visualization in its self-sensing mechanism. This structure skips over raw signal processing and utilizes mechanoluminescence to present strain and damage with brightness variation. Planar DIC, a standardized non-contact method, is performed in this study in parallel with EL luminance analysis to validate the 2D strain and damage field result, while characterizing the spatial resolution of EL luminance method.

Compared to other self-sensing methods which rely on an embedded sensing network, the functional sensing layers proposed in this study is non-intrusive. The additional sensing elements are not embedded within the structural components, which causes variation in structural mechanical properties. In this study, the functional EL sensing layers can be implemented on the surface of any existing CFRP parts similar to a simple detachable strain gauge without modifying the structural properties of the CFRP component to achieve visual strain and damage monitoring.

Author statement

Jiefeng Qiu: Conceptualization, Methodology, Formal Analysis, Investigation, Writing- Original Draft, Writing- Review & Editing.

Gerd Grau: Conceptualization, Writing- Review & Editing, Funding Acquisition, Project Administration, Supervision.

Garrett W. Melenka: Conceptualization, Writing- Review & Editing, Funding Acquisition, Project Administration.

Declaration of competing interest

The authors declare that they have no known competing financial interests or personal relationships that could have appeared to influence the work reported in this paper.

Acknowledgments

The authors would like to acknowledge funding support from York University through the Lassonde Undergraduate Research Award (LURA) and the Lassonde Innovation Fund (LIF). Funding for this work is also supported by the Natural Sciences and Engineering Research Council of Canada Canada RGPIN- 2018-05899 and RGPIN-2018-05857.

References

- [1] Forintos N, Czigany T. Multifunctional application of carbon fiber reinforced polymer composites: electrical properties of the reinforcing carbon fibers – a short review. *Compos B Eng* 2019;162:331–43. <https://doi.org/10.1016/j.compositesb.2018.10.098>. October 2018.
- [2] Naito K, Tanaka Y, Yang JM, Kagawa Y. Tensile properties of ultrahigh strength PAN-based, ultrahigh modulus pitch-based and high ductility pitch-based carbon fibers. *Carbon N. Y.* 2008;46(2):189–95. <https://doi.org/10.1016/j.carbon.2007.11.001>.
- [3] Pavement C. Functional properties of a pitch-based carbon fiber – Mortar composite as a thin overlay for. 2019.
- [4] Mao Q, Zhang Y, Guo Y, Zhao Y. Enhanced electrical conductivity and mechanical properties in thermally stable fine-grained copper wire. *Commun. Mater.* 2021; 1–9. <https://doi.org/10.1038/s43246-021-00150-1>.
- [5] Melenka GW. Analytical and experimental analysis of tubular braided composites. 2016. p. 1–246.
- [6] Millar J, Mary Q. Carbon fibre microelectrodes 2018;270. [https://doi.org/10.1016/0165-0270\(79\)90039-6](https://doi.org/10.1016/0165-0270(79)90039-6). November 1979.
- [7] Idris MK, Qiu J, Melenka GW, Grau G. Printing electronics directly onto carbon fiber composites: unmanned aerial vehicle (UAV) wings with integrated heater for de-icing. *Eng. Res. Express* 2020;2(2). <https://doi.org/10.1088/2631-8695/ab8e24>.
- [8] Guo Y, Xu Y, Wang Q, Dong Q, Yi X, Jia Y. Enhanced lightning strike protection of carbon fiber composites using expanded foils with anisotropic electrical conductivity. *Compos. Part A Appl Sci Manuf* 2019;117(17923):211–8. <https://doi.org/10.1016/j.compositesa.2018.11.022>.
- [9] Dorigato A, Fredi G, Pegoretti A. Application of the thermal energy storage concept to novel epoxy–short carbon fiber composites. *J Appl Polym Sci* 2019;136(21):1–9. <https://doi.org/10.1002/app.47434>.
- [10] Xia ZH, Curtin WA. Damage detection via electrical resistance in CFRP composites under cyclic loading. *Compos Sci Technol* 2008;68(12):2526–34. <https://doi.org/10.1016/j.compscitech.2008.05.007>.
- [11] Naghipour P, Schneider J, Bartsch M, Hausmann J, Voggenreiter H. Fracture simulation of CFRP laminates in mixed mode bending. *Eng Fract Mech* 2009;76(18):2821–33. <https://doi.org/10.1016/j.engfracmech.2009.05.009>.
- [12] Zhu YK, Tian GY, Lu RS, Zhang H. A review of optical NDT technologies. *Sensors* 2011;11(8):7773–98. <https://doi.org/10.3390/s110807773>.
- [13] Schubert KJ, Brauner C, Herrmann AS. Non-damage-related influences on Lamb wave-based structural health monitoring of carbon fiber-reinforced plastic structures. *Struct Health Monit* 2014;13(2):158–76. <https://doi.org/10.1177/1475921713513975>.
- [14] Aoukili A, Khamlichi A. Damage detection of cracks in carbon fibre reinforced composites by pulsed eddy-current testing. *MATEC Web Conf.* 2018;191:4–7. <https://doi.org/10.1051/mateconf/201819100003>.
- [15] Majumder M, Gangopadhyay TK, Chakraborty AK, Dasgupta K, Bhattacharya DK. Fibre Bragg gratings in structural health monitoring-Present status and applications. *Sensors Actuators, A Phys.* 2008;147(1):150–64. <https://doi.org/10.1016/j.sna.2008.04.008>.
- [16] Zheng K, Chang YS, Wang KH, Yao Y. Improved non-destructive testing of carbon fiber reinforced polymer (CFRP) composites using pulsed thermograph. *Polym Test* 2015;46:26–32. <https://doi.org/10.1016/j.polymertesting.2015.06.016>.
- [17] Sket F, Enfedaque A, Díaz López C, González C, Molina-Aldareguía J, Llorca J. X-ray computed tomography analysis of damage evolution in open hole carbon fiber-reinforced laminates subjected to in-plane shear. *Compos Sci Technol* 2016;133:40–50. <https://doi.org/10.1016/j.compscitech.2016.06.012>.
- [18] Gupta R, et al. A Review of sensing technologies for non-destructive evaluation of structural composite materials. 2021.
- [19] Augustin T. Structural health monitoring of carbon fiber reinforced polymers and carbon nanotube modified adhesive joints via electrical resistance measurement. 2018. p. 1–127. <https://doi.org/10.15480/882.1739>.
- [20] Güemes A, Fernandez-lopez A, Pozo AR. Structural health monitoring for advanced composite structures : a Review. 2020. p. 1–15.
- [21] A. Zarafshani and T. Bach, "Using a planar EIT as a Structural Health Monitoring method to detect and evaluate the damage to CFRP composite used in aerospace structures.". 2021.
- [22] Roh HD, Lee H, Bin Park Y. Structural health monitoring of carbon-material-reinforced polymers using electrical resistance measurement. *Int. J. Precis. Eng. Manuf. - Green Technol.* 2016;3(3):311–21. <https://doi.org/10.1007/s40684-016-0040-4>.
- [23] Kashfudoja M, Ramji M. Composites : Part B Whole-field strain analysis and damage assessment of adhesively bonded patch repair of CFRP laminates using 3D-DIC and FEA. *Compos. PART B* 2013;53:46–61. <https://doi.org/10.1016/j.compositesb.2013.04.030>.
- [24] Khaja SVSM, Murthy MH. Determination of damage evolution in CFRP subjected to cyclic loading using DIC. 2018. p. 1412–25. <https://doi.org/10.1111/ffe.12786>. January.
- [25] Merzkirch M, Foecke T. 10° off-axis testing of CFRP using DIC : a study on strength , strain and modulus. *Compos. Part B* 2020;196(April):108062. <https://doi.org/10.1016/j.compositesb.2020.108062>.
- [26] Dong YL, Pan B. A review of speckle pattern fabrication and assessment for digital image correlation. *Exp Mech* 2017;57(8):1161–81. <https://doi.org/10.1007/s11340-017-0283-1>.
- [27] Wang Y, Wang Y, Wan B, Han B, Cai G, Li Z. Properties and mechanisms of self-sensing carbon nano fi bers/epoxy composites for structural health monitoring.

- Compos Struct 2018;200:669–78. <https://doi.org/10.1016/j.compstruct.2018.05.151>. June.
- [28] Ajovalasit A. Advances in strain gauge measurement on composite materials. 2011. p. 313–25. <https://doi.org/10.1111/j.1475-1305.2009.00691.x>.
- [29] Brown BH, Brown BH. Electrical impedance tomography (EIT): a review Electrical impedance tomography. (EIT): Review 2009;1902(2003). <https://doi.org/10.1080/0309190021000059687>.
- [30] Hassan H, Tallman TN. Failure prediction in self-sensing nanocomposites via genetic algorithm-enabled piezoresistive inversion. 2020. <https://doi.org/10.1177/1475921719863062>.
- [31] Hassan H, Tallman TN. A Comparison of Metaheuristic Algorithms for Solving the Piezoresistive Inverse Problem in Self-Sensing Materials, 21; 2021. p. 659–66. <https://doi.org/10.1109/JSEN.2020.3014554>. 1.
- [32] Ryu D, Castaño N, Bhakta R, Kimberley J. Fracto-mechanoluminescent light emission of EuD 4 TEA-PDMS composites subjected to high strain-rate compressive loading. Smart Mater Struct 2017;26(8):85006. <https://doi.org/10.1088/1361-665X/aa6fde>.
- [33] Ryu D, Castano N. Mechanoluminescent composites towards autonomous impact damage detection of aerospace structures. 2016. <https://doi.org/10.12783/SHM2015/275>. January 2015.
- [34] Pulliam E, Hoover G. Multifunctional Mechano-luminescent-optoelectronic composites for self- SMASIS2017-3977. 2019. <https://doi.org/10.1115/SMASIS2017-3977>. September 2017.
- [35] Ii A, Mindlin RD. A Review of the photoelastic method A Review of the photoelastic method of stress analysis . II * t, vol. 273; 2017. April 2004.
- [36] Qiu J, Idris MK, Grau G, Melenka GW. Fabrication of electroluminescent carbon fiber composite for damage visualization. Manuf. Lett. 2020;24:56–60. <https://doi.org/10.1016/j.mfglet.2020.03.010>.
- [37] Qiu J, Idris MK, Grau G, Melenka GW. Fabrication of electroluminescent carbon fiber composite for damage visualization. Manuf. Lett. 2020;24:56–60. <https://doi.org/10.1016/j.mfglet.2020.03.010>.
- [38] Bigger R, et al. A good practices guide for digital image correlation. Int. Digit. Image Correl. Soc. 2018:94 [Online]. Available: <https://doi.org/10.32720/idics/gpg.ed1>. <http://idics.org/guide/>.
- [39] Chu TC, Ranson WF, Sutton MA, Peters WH. Applications of digital . Image-correlation techniques to experimental mechanics. 1985. p. 232–44. September.
- [40] Pedro F. Characterization of failure strain in fiber reinforced composites : under on-Axis and off-Axis loading. 2021. p. 1–11.
- [41] Nurprasetyo IP, Budiman BA, Afwan AA, Halimah PN, Utami ST, Aziz M. Nonlinear piezoresistive behavior of plain-woven carbon fiber reinforced polymer composite subjected to tensile loading. Appl Sci 2020;10(4). <https://doi.org/10.3390/app10041366>.
- [42] Wang L, Xiao L, Gu H, Sun H. Advances in alternating current electroluminescent devices. Adv Opt Mater 2019;1–30. <https://doi.org/10.1002/adom.201801154>. 1801154.
- [43] J. Wang, C. Yan, G. Cai, M. Cui, A. L. Eh, and P. S. Lee, “Extremely stretchable electroluminescent devices with ionic conductors,” doi: 10.1002/adma.201504187.
- [44] Liang J, Li L, Niu X, Yu Z, Pei Q. Elastomeric polymer light-emitting devices and displays, 7; 2013. p. 3–10. <https://doi.org/10.1038/nphoton.2013.242>. October.